# Finite element analysis of a low modulus Ti-20Zr-3Mo-3Sn alloy designed to reduce the stress shielding effect of a hip prosthesis

Tianyu Jia, Dominique Guines, Doina-Margareta Gordin, Lionel Leotoing, Thierry Gloriant

Journal of the Mechanical Behavior of Biomedical Materials xxx (xxxx) 106640

Contents lists available at ScienceDirect

Journal of the Mechanical Behavior of Biomedical Materials

journal homepage: www.elsevier.com/locate/jmbbm



# Finite element analysis of a low modulus Ti-20Zr-3Mo-3Sn alloy designed to reduce the stress shielding effect of a hip prosthesis

Tianyu Jia [a], Dominique Guines [b], Doina-Margareta Gordin [a], Lionel Leotoing [b], Thierry Gloriant [a,*]

[a] University of Rennes, INSA Rennes, CNRS UMR 6226 ISCR, 35000, Rennes, France
[b] University of Rennes, INSA Rennes, LGCGM, EA 3913, 35000, Rennes, France

ARTICLE INFO

*Keywords:*
Titanium alloys
Low modulus
Stress shielding
Hip prosthesis
Finite element analysis

ABSTRACT

After total hip arthroplasty, the stress shielding effect can occur due to the difference of stiffness between the metallic alloy of the stems and the host bone, which may cause a proximal bone loss. To overcome this problem, a low-modulus metastable β Ti-20Zr-3Mo-3Sn alloy composition has recently been designed to be potentially used for the cementless femoral hip stems. After having verified experimentally that the β alloy has a low modulus of around 50 GPa, a finite element analysis was performed on a Ti-20Zr-3Mo-3Sn alloy hip prosthesis model to evaluate the influence of a reduced modulus on stress shielding and stress fields in both stem and bone compared with the medical grade Ti-6Al-4V alloy whose elastic modulus reached 110 GPa. Our results show that the Ti-20Zr-3Mo-3Sn stem with low elastic modulus can effectively reduce the total stress shielding by 45.5% compared to the common Ti-6Al-4V prosthesis. Moreover, it is highlighted that the material elasticity affects the stress distribution in the implant, especially near the bone-stem interfaces.

## 1. Introduction

Nowadays, the total hip arthroplasty (THA) is a widespread surgical procedure, beneficial to restore hip joint mobility for patients suffering from trauma or joint diseases. However, the femur starts to degrade after some years because of its deficient loading (Head et al., 1995; Huiskes et al., 1992; Tanzer et al., 2001). According to Wolff's law, the bone structure chronically adjusts to the force acting on it. In underloaded zones, bone reacts by reducing bone mass, which is known as bone resorption. This phenomenon can cause the implant to loosen (Bugbee et al., 1996; Huiskes et al., 1992; Van Rietbergen et al., 1993). The etiology of bone resorption is multifactorial (Gillies et al., 2007; Sychterz and Engh, 1996), but it is mainly caused by a reduction in load transmission from implant to bone; this is the so-called "stress shielding effect" (Van Rietbergen et al., 1993). As a result, the rigidity of the implant is predominant since if it is too high, the mechanical load will not be correctly transferred to the surrounding bone. The stress shielding can be quantified by evaluating the stress difference between the implanted femur and the non-implanted femur. A volume-averaged stress shielding rate is then defined as a change in strain energy in the implanted bone compared to the reference value of the intact bone (Alkhatib et al., 2019; Arabnejad et al., 2017; Huiskes et al., 2000; Weinans et al., 2000). It is important to underline that the values of stress shielding are usually evaluated immediately after the operation, but not necessarily for a long-term state.

The most widely used implant materials are 316L stainless steel, Co-Cr and Ti-6Al-4V ELI alloys, whose Young's moduli are close to 180 GPa, 210 GPa and 110 GPa, respectively. The order of magnitude of Young's moduli for pure titanium and its alloys is lower than those of stainless steels and Co-Cr alloys but it nevertheless remains much higher than those of cortical and trabecular bones, ranging from 15 to 24 GPa (Morgan et al., 2018; Rho et al., 1993; Weinans et al., 2000).

To find an appropriate compromise between good implant fixation and minimization of stress shielding effect, some attempts on developing new implant materials have been made such as using modulus-gradient stems (Baba et al., 2023; Yamako et al., 2017), proposing porous alloys (Cortis et al., 2022; Naghavi et al., 2023; Sun et al., 2018), modifying surface textures (Chyr et al., 2014) and designing lattice structured stems (Harrison et al., 2013; Jetté et al., 2018). For instance, a cementless Ti-33.6Nb-4Sn stem was developed with the elastic modulus graded from the proximal (82.1 GPa) to the distal end (51.0 GPa) (Hanada et al., 2014). To assess the stress shielding of the implanted bone, equivalent strains on the cortical surfaces were measured by bonding strain-gage rosettes onto the composite femurs and compared with the values of the intact bones (Yamako et al., 2014). The modulus-graded Ti-33.6Nb-4Sn stems gave positive results in the reduction of

* Corresponding author.
*E-mail address:* Thierry.Gloriant@insa-rennes.fr (T. Gloriant).

https://doi.org/10.1016/j.jmbbm.2024.106640
Received 28 February 2024; Received in revised form 17 June 2024; Accepted 19 June 2024
1751-6161/

stress shielding compared to the typical Ti-6Al-4V stems, especially in the proximal calcar regions (around 83% and 85% stress subjected by of the intact cortical bone). Based on the bone remodelling theory (Huiskes et al., 1992; Weinans et al., 1992), the predicted results concluded that the bone mineral density for the Ti-33.6Nb-4Sn stems would be 142.6% of that for Ti-6Al-4V stems after 10 years (Yamako et al., 2017).

In addition to the stress shielding effect, another issue arises in the implant stability and hence the bone-prosthesis interaction. For cementless implants, the connection between the implant and femur affects their fixation and the clinical success of the arthroplasty. Although cementless prostheses evoke a higher revision rate than the cemented cases in the elderly (over 75 years old) female group, the increasing use of uncemented fixation makes it mainstream around the world (Troelsen et al., 2013). The influence of bone-stem contact on the movement and cyclic motions has been studied experimentally and by finite element analysis (Dammak et al., 1997; Kuiper and Huiskes, 1996; Shirazi-Adl et al., 1993; Zhang et al., 1999). The influence of the coefficients of friction was first studied with a 2D finite element model of a cementless stem (Kuiper and Huiskes, 1996). It was shown that a frictional implant-bone contact could greatly reduce the cyclic motion by about 85% compared to a frictionless case. However, the femoral stress field seemed to be insensitive to the value of the friction coefficient (Kuiper and Huiskes, 1996). The value of the friction coefficient between a porous tantalum stem with the surrounding bone was experimentally determined between 0.74 and 1.75, depending on the preparation methods (Zhang et al., 1999). However, due to the long-term bone in-growth, the implant may be perfectly bonded to the bone but this is not the case for the immediate post implantation state. Based on the previous studies, assuming either a perfect bonded or a frictionless interface is inappropriate to evaluate the post-implantation performances. To author's knowledge, the influence of bone-stem friction on the stress shielding effect is rarely investigated.

Recently, our team developed a novel β-type Ti-20Zr-3Mo-3Sn (at.%, Ti2033) alloy composition, which consists of toxicity- and allergy-free elements and exhibits a low Young's modulus after specific heat treatment (Gao et al., 2019). Firstly, a new Ti2033 ingot has been prepared in the lab to check the microstructural and mechanical characteristics of the alloy. Then, based on these experimental data, a finite element (FE) modelling was performed on a Ti-20Zr-3Mo-3Sn alloy hip prosthesis model to evaluate the influence of a reduced modulus on stress shielding and stress fields in both stem and bone and compared with the medical grade Ti-6Al-4V ELI alloy (wt.%, Ti64). More specifically, this is the first to comprehensively investigate the effects of implant elasticity, considering nine different materials, alongside friction at the bone-stem interface, across six cases. These effects are quantified by evaluating the implant movements, femoral stress shielding and the level of interface stresses. Notably, our simultaneous discussion of implant elasticity and interfacial friction is a unique feature which is not commonly found in other finite element method studies.

## 2. Materials and methods

### 2.1. Implant materials

Ti-6Al-4V ELI grade (wt.%, Ti64) is a commercial material for femoral prostheses because of its high strength properties and biocompatibility with human body. To elaborate the Ti2033 alloy, the raw metals were first melted by cold crucible levitation melting under argon atmosphere. A homogenization treatment was applied to the ingot at 950°C for 1200 min under high vacuum ($10^{-7}$ mbar), followed by a water quenching. The ingot was then cold-rolled at room temperature to obtain a sheet reduced to 95% of the initial thickness. In order to characterize the mechanical behaviour of the material, tensile specimens with thicknesses of 2 mm and gauge sections of $3 \times 15$ mm$^2$ were cut from the cold-rolled sheet. Those specimens were finally solution-treated at 900°C for 30 min under high vacuum ($10^{-7}$ mbar), followed by a water quenching to obtain a fully cubic body centred β microstructure at room temperature.

X-ray diffraction (XRD) and Electron back-scattered diffraction (EBSD) analyses were conducted to characterize the microstructure of Ti2033 after solution treatment. Before EBSD observations, all samples were mechanically mirror-polished by using several SiC papers with decreasing grid size, followed by colloidal silica suspension. In the obtained EBSD inverse pole figures (IPF), RD and ND refer to the rolling direction (parallel to the loading direction for tensile tests) and to the normal direction, respectively. Fig. 1 shows that a principal $<113>_\beta\{110\}_\beta$ texture and a slight $<110>_\beta\{111\}_\beta$ texture are obtained in the Ti2033 specimen with a typical equiaxed β-grain microstructure. By XRD study, the typical diffraction peaks of the cubic body centred β phase, $(110)_\beta$, $(002)_\beta$, $(112)_\beta$, $(202)_\beta$ and $(013)_\beta$ are clearly observed (Fig. 2).

Tensile tests were performed at room temperature until fracture, under quasi-static conditions (strain rate of $10^{-4}$ s$^{-1}$). An extensometer was used for strain measurements. Specimens are loaded along the cold rolling direction. In Fig. 3, the stress-strain curves for Ti2033 and medical grade Ti64 specimens are displayed. It can be observed that the Ti2033 alloy exhibits a much lower Young's modulus, around 50 GPa, a lower yield strength, and a higher elongation at rupture compared to Ti64. All these characteristics are in agreement with the results of a study recently carried out in our laboratory on this alloy (Gao et al., 2019).

### 2.2. Femur

The femur was modelled as a homogeneous material with mechanical properties corresponding to a cortical bone: Young's modulus rang-

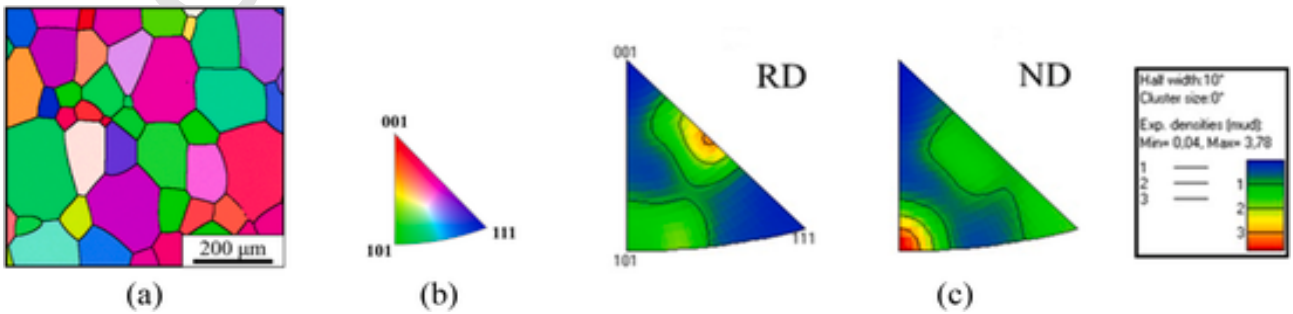


**Fig. 1.** EBSD results of solution treated Ti2033 specimens at 900°C for 30 min. Inverse pole figure (IPF) map (a) along RD, (b) corresponding colour code, (c) RD and ND inverse pole figures.

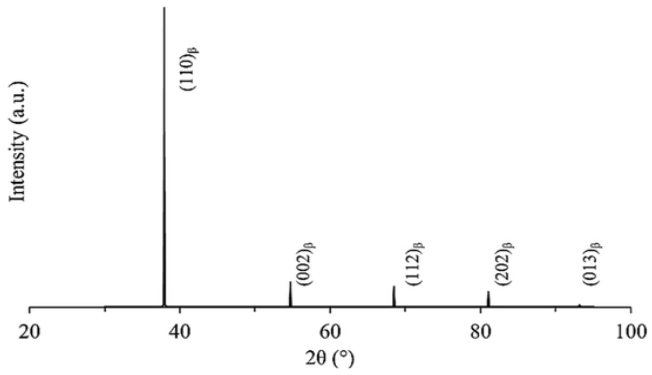


**Fig. 2.** XRD profile of the solution treated Ti2033 alloy.

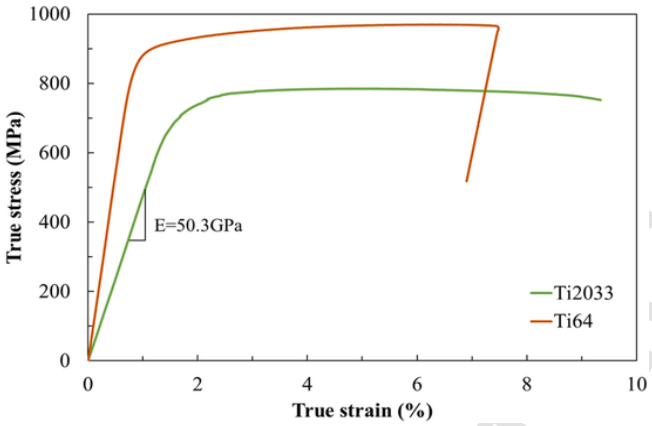


**Fig. 3.** True stress-strain tensile curves of Ti2033 (green) and Ti64 (orange) specimens until fracture.

ing from 15 GPa to 24 GPa (Morgan et al., 2018; Rho et al., 1993; Weinans et al., 2000) and Poisson's ratio ranging from 0.25 to 0.4 (Cristofolini et al., 2009; Grassi et al., 2013; Helgason et al., 2008). Herein the Young's modulus and Poisson's ratio are set to 18 GPa and 0.3, respectively. The mechanical characteristics of both femur and prosthesis materials (Ti64 and Ti2033) are summarised in Table 1. Besides, in order to evaluate the effect of the value of the Young's modulus on the femur performance, different constitutive materials of the implant with various elastic moduli are introduced. They are named "EX" with "X" corresponding to the value of the Young's modulus, for instance, E30 refers to a virtual material whose elastic modulus equals 30 GPa. The Poisson's ratio is assumed to be 0.3 for all the materials. The mechanical behaviour of the bone and implants is assumed to be isotropic (Naghavi et al., 2023).

**Table 1**
Mechanical characteristics of the femur, Ti2033 and Ti64.

| Parts | Material | Density ($g/cm^3$) | E (GPa) | Poisson's Ratio | Yield Stress (MPa) |
|---|---|---|---|---|---|
| Implant | Ti-20Zr-3Mo-3Sn | 5.07 | 50.3 | 0.3 | 780 |
| | Ti-6Al-4V ELI | 4.43 | 110 | 0.3 | 900 |
| Femur | Cortical bone | 1.8 | 18 | 0.3 | 150 |

## 3. Prosthesis design and modelling

### 3.1. Prosthesis design

The left femur model refers to an open access research (Moshfeghifar et al., 2022) in Fig. 4(a). The hip prosthesis is designed as a long stem with a femoral head connected by a neck made of titanium alloy like that of the stem. Although ceramic heads are preferred thanks to their superior wear performance, it is the neck part, which connects the head and the stem, that facilitates the movement of head. The head material is not the vital factor in stem deformation due to the minimal strain in head zone. The dimensions of the prosthesis are given in Fig. 4 (a). As shown in Fig. 4(b), the stem axis is aligned with the y-axis of the global coordinate system, pointing upward, the x-axis is pointing from the centre of pelvis, and the z-axis is consequently according to left-handed system. According to a relative study (Cortis et al., 2022), the femoral neck osteotomy angle is 140° and the anteversion angle between y-axis and the neck shaft axis is 9°. The entire femur and prosthesis were meshed by 232,283 and 59,597 linear tetrahedron elements, respectively. A global size of 2 mm is applied after a convergence study on the final displacement at the head centre and maximum von Mises stress distribution. The final mesh is shown in Fig. 4(c).

### 3.2. Interaction

To investigate a straightforward effect of the implant material, no bone cement is involved in this study. The press-fit fixation of the cementless implant in the femur is applied in this work, which is commonly chosen for the hip joint replacement surgeries. The press-fit prosthesis allows gradual bone in-growth to reach enough stability after 6–8 weeks. Hence, the interaction between the implant and the bone keeps varying during the period. The coefficient of friction between the cementless implant and the bone has been reported from 0.08 to 1.6, depending on the surface conditions (Table 2). Therefore, a surface-to-surface contact is built between the implant and femur and different values of friction coefficients are defined from 0.25 to 1.5. Normal contact is considered as hard contact (Yamako et al., 2017).

### 3.3. Boundary conditions and loading

An encastre condition is defined on nodes belonging to intercondylar fossa. Loading of a walking gait (toe off) is considered in this study (Yamako et al., 2017), which involves hip contact force, abductor muscle force and vastus lateralis force, as shown in Fig. 5. All the forces are applied to the reference points P0, P1 and P2, kinematically coupled with neighbouring nodes. The values of forces are given in Table 3.

### 3.4. Stress-shielding rate

The stress shielding rate (SSR) is a concept based on the calculation of the difference of the stored strain energy between a reference configuration and after implantation (Beaupré et al., 1990; Weinans et al., 2000). In this study, the reference configuration corresponds to an implant material identical to the one of cortical bone.

For linear isotropic materials undergoing small deformation, the strain energy density in an element is defined as:

$$SEDEN = \frac{1}{2}\left(\sigma_{xx}\varepsilon_{xx} + \sigma_{yy}\varepsilon_{yy} + \sigma_{zz}\varepsilon_{zz}\right) + \left(\sigma_{xy}\varepsilon_{xy} + \sigma_{yz}\varepsilon_{yz} + \sigma_{zx}\varepsilon_{zx}\right). \quad (1)$$

The strain energy (SE) in a specific zone is the summation of that in each element (Eq. (2)). In each element, strain energy is calculated from the product of strain energy density (SEDEN) and element volume:

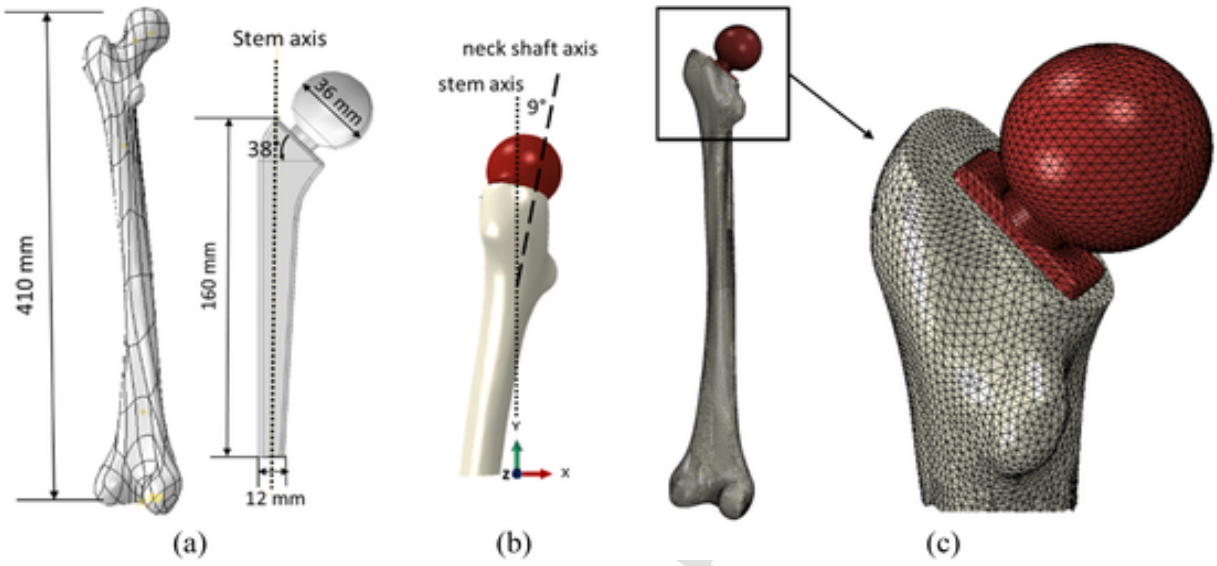


**Fig. 4.** The model consists of (a) an open-access 3D femur and a long stem. (b) Shows the anteversion angle between y-axis and the neck shaft axis. (c) Is the mesh pattern.

**Table 2**
Bone-implant interaction.

| Friction value | Surface conditions |
|---|---|
| Fully bonded | Perfect bone in-growth |
| 0.08 | Polished surface (Reimeringer and Nuño, 2016) |
| 0.15 | Lubricant by mixture of blood and marrow acts (Kuiper and Huiskes, 1996) |
| 0.3 | Smooth surface (ten Broeke et al., 2014) |
| 0.4 | Smooth titanium plate and wet bone (Shirazi-Adl et al., 1993) |
| 0.6 | Plasma-spray surface with bone (Reimeringer and Nuño, 2016) |
| 0.88 | Porous tantalum with bone (Zhang et al., 1999) |
| 1.3–1.6 | OsteoAchor stem with bone (Harrison et al., 2013) |

$$SE = \sum_{i=0}^{n} SEDEN \bullet V_i, \tag{2}$$

where n is the total number of femur elements, and $V_i$ is the element volume. The stress shielding rate is defined as:

$$SSR = \frac{SE_{reference} - SE_{implanted}}{SE_{reference}}. \tag{3}$$

### 3.5. Test configurations

A static implicit analysis is completed with the FE commercial software Abaqus/Standard 2021. Finally, eighteen FE configurations are performed, employing cortical bone (CB), Ti2033 and Ti64 as implant materials, with six different coefficients of friction (CF = 0.25, 0.5, 0.75, 1.0, 1.25, 1.5) to study friction effects. Sixteen FE analyses are carried out using prostheses made from eight different virtual materials with different moduli varying between 30 and 100 GPa (E30, E40, E60, E70, E80, E90 and E100) under two specific friction conditions (CF = 0.75 and CF = 1.25), to study the effect of material rigidity.

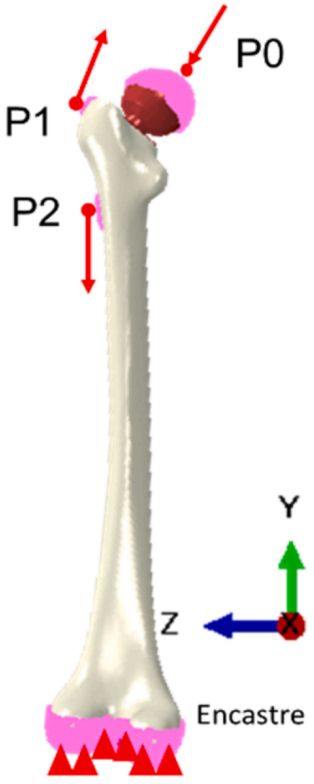


**Fig. 5.** Loading and boundary conditions applied to the FE model. Forces are applied on the reference points (red dots) kinematically coupled with neighbouring nodes (pink regions).

## 4. Results & discussion

### 4.1. Movement of the femoral head & micromotion

The movement of the femoral head is critical factor for implant stability. Excessive displacement can cause dislocation after implantation,

**Table 3**
Loading condition of a walking gait (toe off) (Yamako et al., 2017).

| Load | Description | $F_x$ (N) | $F_y$ (N) | $F_z$ (N) |
|---|---|---|---|---|
| P0 | Hip contact | −263 | −1833 | −432 |
| P1 | Abductors | 122 | −646 | −518 |
| P2 | Vastus lateralis | 148 | −743 | −7 |

necessitating revision surgery, where the ball of the new hip implant comes out of the socket.

Fig. 6(a) illustrates the evolution of the maximum displacement of the femoral head with six different friction coefficients, using the two implant materials (Ti64, Ti2033), and the reference case of cortical bone. The effect of friction coefficient on the maximum displacement of the prosthesis is not significant.

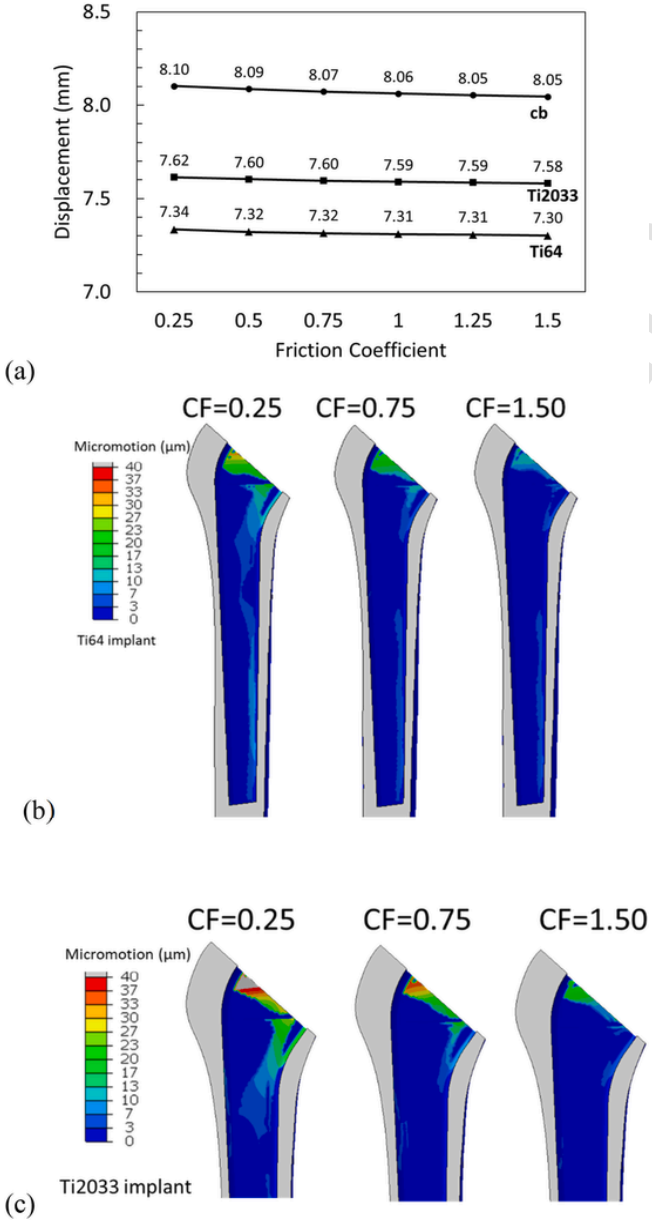


**Fig. 6.** Movement of the implants under different frictional cases: (a) femoral head displacement of three implant materials, micromotion at the bone-stem interface with (b) a Ti64 implant and (c) a Ti2033 implant.

Moreover, a previous study (Bennett and Goswami, 2008) reported that the maximal displacements of six stem designs using Ti64, CoCrMo and stainless steel ranged from 4 to 17 mm under a 2500N total load. This study also drew the same conclusion concerning the relationship between implant elasticity and femoral head displacement. The Ti2033 stem results in a displacement 3.8% larger than the one corresponding to Ti64, which is not statistically significant.

The first stability of implants lies in bone-implant micromotions, that is, relative movements between the implant and bone tissue (Pilliar et al., 1986). This study focuses on the immediate postoperative micromotion at a smooth bone-implant interface, setting an allowable threshold of 40 μm. Given that bone osseointegration occurs when micromotions remain below 40 μm and becomes unlikely with a micromotion greater than 150 μm (Jasty et al., 1997), the chosen micromotion threshold provides a reliable and conservative assessment of implant stability. The summation of the tangential micromotions is presented in Fig. 6(b) and (c) for the Ti64 and Ti2033 implants, respectively. The medial and distal micromotion distributions after inserting Ti2033 implants are suppressed for exhibition due to the very similar distributions, regardless of friction. The decrease of micromotions at the interfaces are observed with increasing bone-stem friction and implant elasticity, indicating better primary stability of implants. Most of the micromotion values fall within the allowable range. The maximum micromotion occurred at the minimum friction (CF = 0.25), and the values for the E30, Ti2033, and Ti64 implants were 85, 51, and 39 μm, respectively. The portions where micromotions exceed the allowable range are marginal in low-modulus implants. Those portions are predominantly concentrated in the proximal regions, in agreement with other findings (Viceconti et al., 2006).

### 4.2. Stress shielding rate assessment

To assess the stress shielding rate, the stem geometry is partitioned into seven Gruen zones (Fig. 7(a)), a method first proposed by Gruen (Gruen et al., 1979) and commonly used in the recent years (Alkhatib et al., 2019; Cortis et al., 2022; Jetté et al., 2018; Yamako et al., 2017). While some studies neglect the effect of strain and simplify the evaluation to consider only the von Mises stress distribution (Joshi et al., 2000; Naghavi et al., 2023), we find that calculating the strain energy density is essential to explore stress shielding in such stem design.

Then, Fig. 7(b) presents the stress shielding results for Ti2033 and Ti64 stems under different friction cases. Although there is a slight difference observed in Gruen zones 1 (4.8% and 4.13% for the Ti2033 and Ti64 implants, respectively) and 3 (2.3% and 4.56% for the Ti2033 and Ti64 implants, respectively) on the lateral side, changes in SSR values with frictional conditions are generally not significant for a given implant material. Thus, it can be deemed that changes in friction coefficients have minimal influence on the stress shielding, regardless of the implant material.

The SSR results for all virtual implant materials (CF = 0.75) are presented in Fig. 8. In general, Fig. 7 (b) and Fig. 8 both reveal higher SSR values in the proximal and medial regions (Gruen zones 1, 2, 6, and 7) compared to the distal regions, consistent with observations from radiological studies (Kärrholm et al., 2002; Rivière et al., 2018). Besides, SSR values in the Gruen zone 4 are negligible for all implants. On the lateral side, the maximum SSR result is observed in the Gruen zone 2. On the medial side, the SSR result decreases from the proximal (Gruen zone 7) to the distal regions (Gruen zone 6, 5), in agreement with prior studies (Alkhatib et al., 2019; Naghavi et al., 2023; Yamako et al., 2017).

Fig. 8 reveals a noteworthy nonlinear decline in the SSR values within the proximal and medial Gruen zones 1, 2, 6 and 7 as the Young's moduli of the implants decreases. The decreasing rate of SSR in these zones accelerates for values of implant Young's modulus exceeding 80 GPa. In contrast, the SSR evolution in the distal Gruen

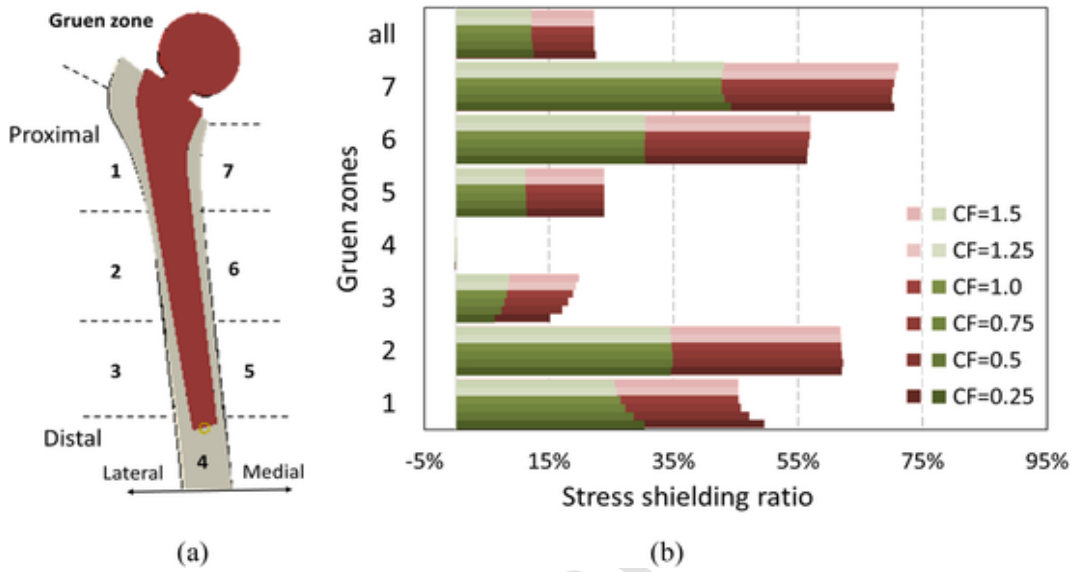


**Fig. 7.** SSR results for all friction cases: (a) based on the configuration of Gruen zones in the femur; (b) using Ti2033 (green) and Ti64 (red) stems. Colour density decreases with the friction coefficient.

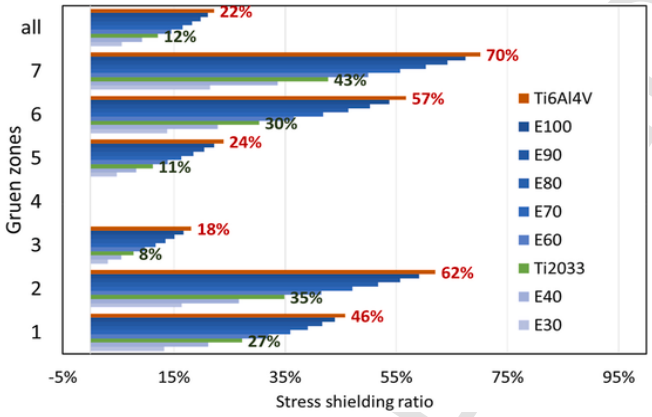


**Fig. 8.** SSR results for all virtual materials (CF = 0.75).

zones 3 and 5 follows an approximately linear pattern with changes in the elastic rigidity of the implant materials. Comparing the Ti2033 and E30 implants with the Ti64 implant, there is a reduction in SSR of 41%, 44%, 57%, 53%, 46%, and 39% for Gruen zones 1 to 7 (zone 4 excluded) for Ti2033 and by 74%, 74%, 82%, 80%, 75%, and 70% for E30. Overall, the total stress shielding rates induced by Ti2033 and E30 prostheses are 55% and 26% of those induced by the Ti64 prosthesis across all Gruen zones. Noteworthily, it is essential to eliminate the stress shielding and meanwhile maintaining stability of the implants. Therefore, the low-modulus Ti2033 offers a compromise that can lessen almost half of the stress shielding induced by the conventional Ti-6Al-4V stems while guaranteeing adequate stability.

### 4.3. Von Mises stress distribution

As previously mentioned, a reference case using cortical bone material for the prosthesis was conducted to study the effect of friction coefficient on the stress distribution at the interfaces. From the major principal strain graph of the left femur in Fig. 9 (a), it is overserved that the nodes on the lateral side are in a tensile state, while the nodes on the medial side are in a compression state. The von Mises stress values across the entire bone are below the yield strength. Two paths of interface nodes on the centre lines of the two contact surfaces (lateral and medial) are delineated (Fig. 9 (a)).

As displayed in Fig. 9 (b), only minor differences in the von Mises stress along Path-1 are observed with different friction coefficients in the proximal zone, but on a relatively small scale compared to Path-2. For instance, with a coefficient of friction of 1.5, the von Mises stress value along Path-2 decreases from 28 MPa to 10 MPa in the proximal region, then increases towards the diaphysis and drops until the end. The same tendency is observed for all frictional cases. The von Mises stress along Path-2 in the Gruen zone 7 increases with higher coefficients of friction, with the increasing rate slowing down towards the Gruen zone 6. Compared to the smallest friction coefficient (CF = 0.25), the largest one leads to an approximate 41% increase of in the von Mises stress near the proximal end of Path-2. However, the von Mises stress distribution seems insensitive to changes in the bone-stem friction in other regions. Other studies reported very similar stress distributions for the contact surfaces with both varied friction and the perfect bond cases, when the bone-implant friction was assigned from zero to a perfect bonded case (Fraldi et al., 2010). Moreover, a similar result highlighted the low influence of the friction coefficient on the final amount of ingrowth (Fernandes et al., 2002). It is concluded that increasing the friction coefficients between the implant and bone may merely raise the stress in the proximal part of the femur.

Given the minimal role of the friction coefficient in both stress shielding rate and stress distribution, four transversal cut planes are defined (Fig. 10 (a)) to analyse the transversal mises stress distribution for the reference case (CB case). The stress patterns were visualized with a scale from 0 to 70 MPa in Fig. 10 (b) and (c). As expected, the stress patterns on the Cut planes-II, III and IV were remarkably similar regardless of frictional coefficients. Therefore, only results for the Cut plane-I are displayed in Fig. 10 (c).

Five nodes on the Cut plane-I were selected, including N1 and N5 in the femur and N2, N3, and N4 in the stem, as illustrated in Fig. 10. The von Mises stresses at these selected five points on the Cut plane-I are plotted in Fig. 10 (d). Notably, there is no apparent difference in the stress values of N1 and N5 located in the femur. However, for the points in the stem N2, N3 and N4, the von Mises stress decrease is respectively about 9.3 MPa, 4 MPa and 10.2 MPa, as the friction coefficient changes from 0.25 to 1.5. Although there is a similar decreasing tendency in the

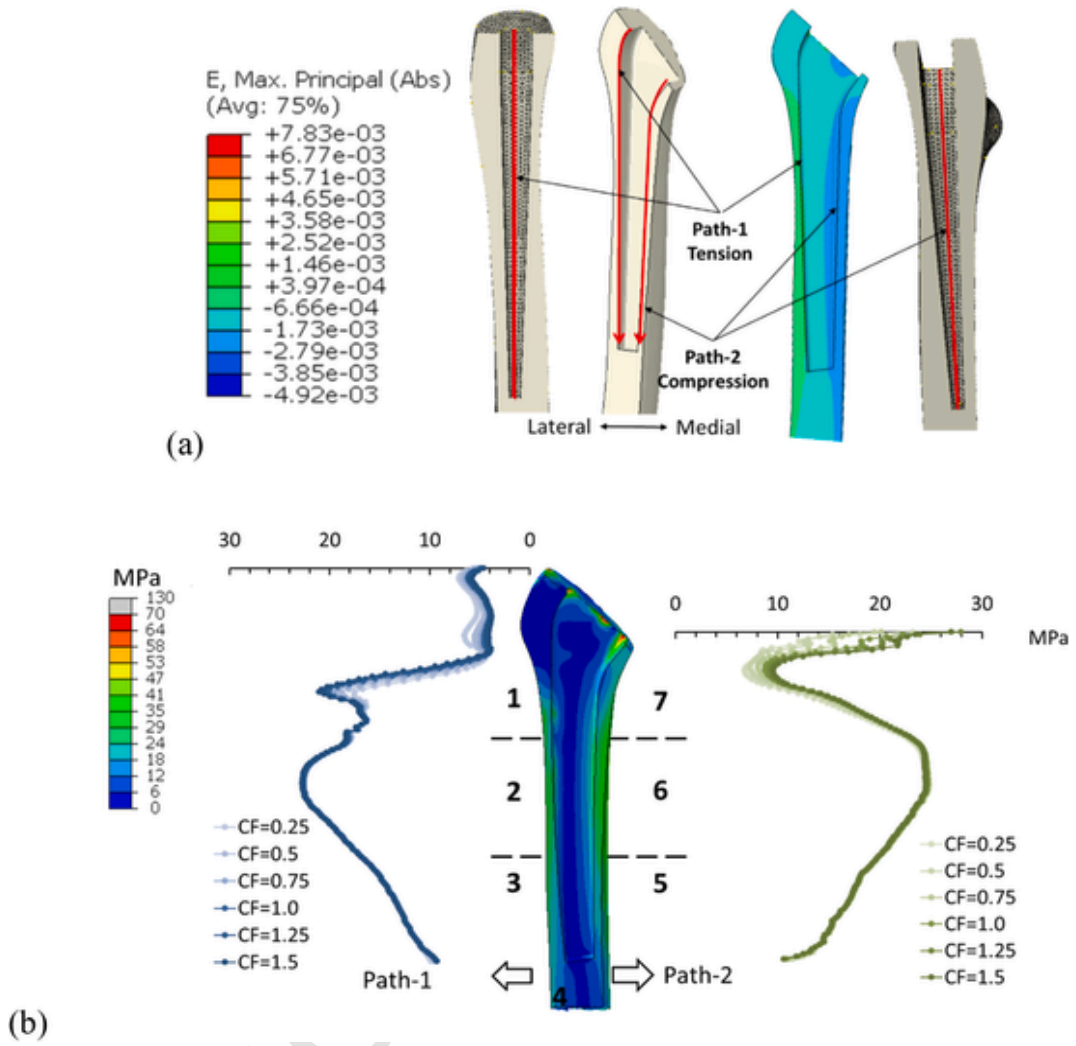


**Fig. 9.** Results for the reference case. (a) Distribution of the major principal strain in the femur and definitions of Path-1 and Path-2; (b) Evolution of the von Mises stress along the two paths with different friction coefficients. Colour density increases with the friction coefficient.

stress of the points in the prostheses, an opposite decreasing rate is observed for the two points close to the bone-stem interface, N2 and N4.

Fig. 11 shows the stress distribution for the CB, Ti2033 and Ti64 prostheses on the sagittal cross-section planes and four transversal Cut planes defined in Fig. 10. Fig. 11 notably, both Ti64 and Ti2033 prostheses are subjected to larger stress than the surrounding femur, correlated to the existence of a stress shielding effect. In comparison with the Ti64 material, Ti2033 permits a reduction of the stress in the stem, transferring more load to the proximal bone, as shown in Fig. 11 (a). A smaller stress localization is evident at the bone-Ti2033 stem interface compared to the Ti64 stem on the Cut planes I, II and III in Fig. 11 (b). In Fig. 12, von Mises stress values for the same five points on Cut plane-I are plotted for the studied implants. As the coefficient of friction changes from 0.75 to 1.5, the N1, N3 and N5 stress presents no significant variations. However, the stress in Ti2033 and Ti64 stem decreases by 10.2% and 6.2% for N2, 17% and 7% for N4, respectively. With a friction coefficient of 1.5, the N2 and N4 stress values for the Ti64 stem are 32 MPa and 47 MPa higher than those for the CB stem, while for the Ti2033 stem, they are 19 MPa and 24 MPa higher, respectively.

A typical 'spot-weld' phenomenon for the immediate post-implantation occurred at the stem interface (red marks in Fig. 11), which involves the development of new bone from the endosteal surface that extends toward the prosthesis. This phenomenon is predominantly observed in cementless femoral stems and serves as a robust indicator of stability (Engh et al., 1987). A stiffer prosthesis involves more severe stress localizations at the bone-stem interface, as shown in Fig. 11, which is associated with prosthesis loosening (Mjöberg, 1997).

Finally, several limitations of the current study should be expounded. Firstly, the femur is modelled without tissues at the bone-stem interface. Incorporating tissue differentiation could enhance the accuracy of predicting bone behaviour post-implantation. Nevertheless, given that cortical bone is the stiffest part in a femur, the conclusions about the effects of the stem elastic rigidity on stress shielding rate remain valid. Secondly, our analysis only considers one loading configuration of walking (toe off) with the action of major muscle forces was included, which can be broadened to multiple physiological cases such as bending knees and climbing stairs. Moreover, the Ti2033 alloy is a high Zr-containing β-Ti alloy. Given the inhibition effect of high Zr content on calcium phosphate precipitation, the reduced calcium phosphate precipitation may result in a smoother bone tissue surface, thereby reducing friction with the surface of the artificial hip joint. There are various options to enhance the implant fixation by increasing the friction coefficient of the bone-implant interface, such as using grid-blast technique, or by promoting precipitation of calcium phosphate on the implant surfaces. Finally, to track the long-time response of the fe-

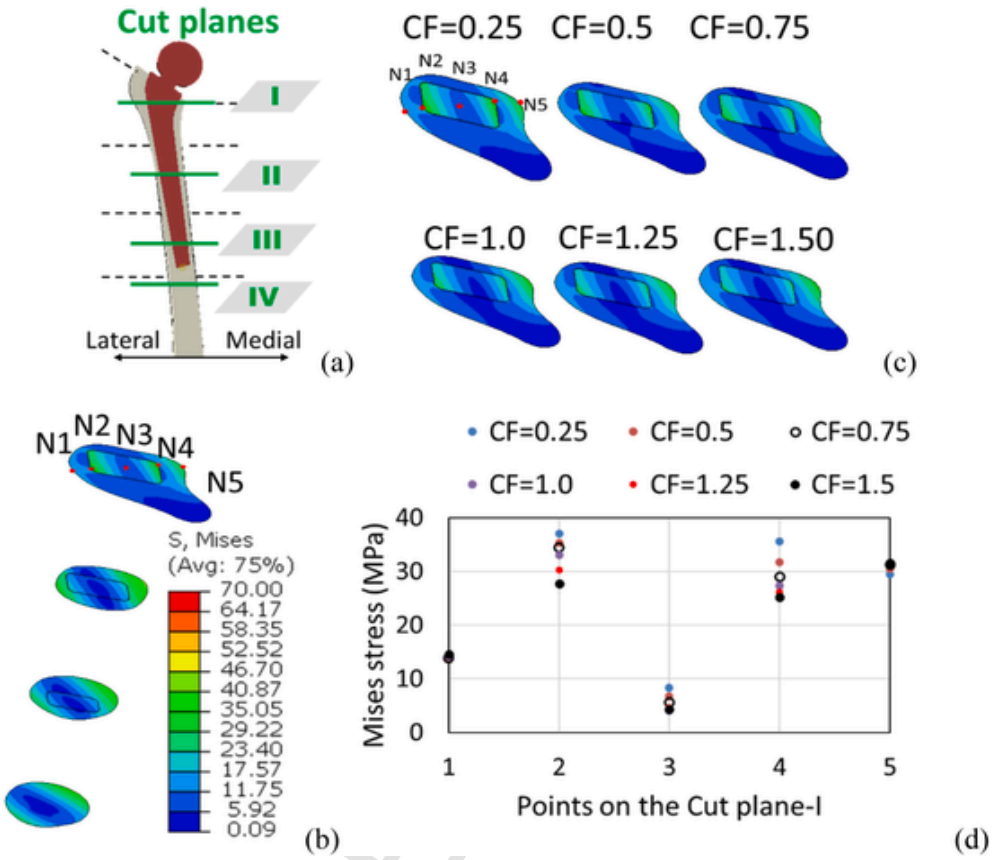


**Fig. 10.** (a) Configurations of the transversal Cut Planes; (b) Von Mises stress distribution for all the cut planes (CF = 0.25) (c) Influence of the value of the friction coefficient on the stress distribution; (d) Evolution of the von Mises values for the five selected points.

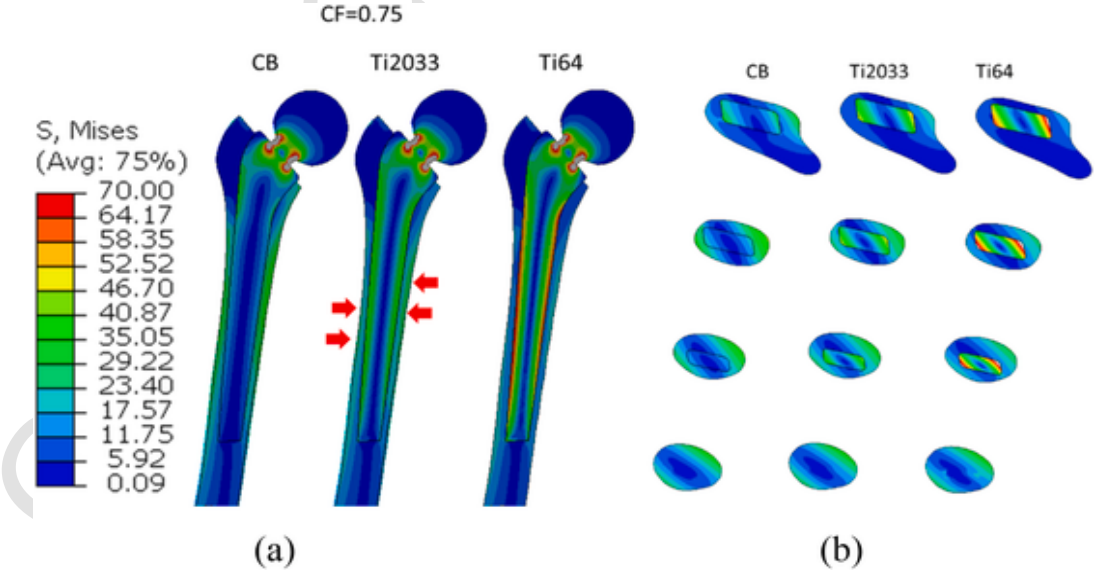


**Fig. 11.** Von Mises stress distribution (CF = 0.75) on the sagittal cross-sections and transversal Cut planes for different implant materials: CB, Ti2033 and Ti64.

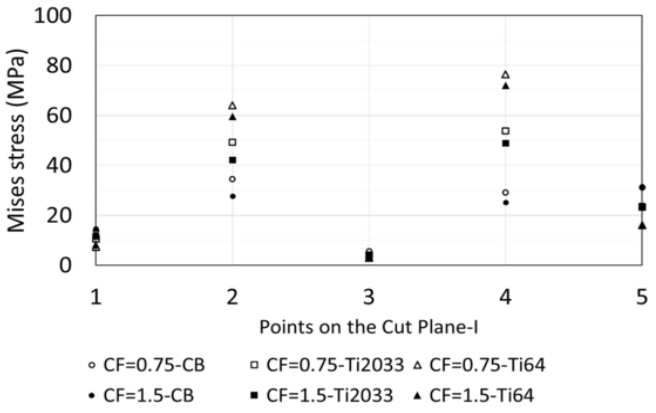


**Fig. 12.** Von Mises stress value for the five selected points (from N1 to N5) on Cut plane-I.

mur post implantation, it would be beneficial to study the structural fatigue and bone-remodelling over elongated time, corresponding to several years.

## 5. Conclusion

A low modulus Ti-20Zr-3Mo-3Sn alloy was manufactured by cold crucible levitation melting in the present study. The alloy, consisting of a fully body centred cubic β microstructure, has a much lower Young's modulus, around 50 GPa, compared to the classical Ti-6Al-4V ELI alloy (110 GPa). Thanks to this low modulus, the alloy is promising for the manufacture of hip prostheses in order to overcome the stress shielding problem.

Based on results from the finite element modelling of the prostheses implanted into the femur, frictional changes between the bone and the implant have only a very limited effect on the stress shielding. A larger friction coefficient may increase the stress in the proximal bone at the contact interface, which is a positive response to the bone. Furthermore, it is demonstrated that elastic rigidity of the prosthetic material has a major effect on post-implantation stress shielding rate. Substituting the classical Ti-6Al-4V ELI alloy with low modulus Ti-20Zr-3Mo-3Sn alloy can effectively reduce the incompatible bone-stem stress transfer and also reduce the total stress shielding rate by 45.5%.

In conclusion, although stress shielding is not completely eliminated, there is a tendency to transfer more loads to the femur after the implantation of Ti-20Zr-3Mo-3Sn stem without compromising initial stability. The Ti-20Zr-3Mo-3Sn alloy exhibits promising characteristics, positioning it as a potential candidate for crafting cementless femoral prostheses to substitute those traditionally made from the Ti-6Al-4V medical grade. In our forthcoming investigations, our focus will be on minimizing stress shielding by refining the prosthetic shape and enhancing implant fixation.

## CRediT authorship contribution statement

**Tianyu Jia:** Writing – original draft, Validation, Software, Methodology, Investigation, Formal analysis. **Dominique Guines:** Validation, Software, Methodology, Investigation. **Doina-Margareta Gordin:** Validation, Investigation. **Lionel Leotoing:** Writing – original draft, Supervision, Methodology, Investigation. **Thierry Gloriant:** Writing – review & editing, Validation, Supervision, Project administration, Investigation, Conceptualization.

## Declaration of competing interest

The authors declare that they have no known competing financial interests or personal relationships that could have appeared to influence the work reported in this paper.

## Data availability

Data will be made available on request.

## References

Alkhatib, S.E., Mehboob, H., Tarlochan, F., 2019. Finite element analysis of porous titanium alloy hip stem to evaluate the biomechanical performance during walking and stair climbing. J. Bionic Eng. 16, 1103–1115. https://doi.org/10.1007/s42235-019-0122-4.

Arabnejad, S., Johnston, B., Tanzer, M., Pasini, D., 2017. Fully porous 3D printed titanium femoral stem to reduce stress-shielding following total hip arthroplasty: fully porous 3D printed titanium femoral stem. J. Orthop. Res. 35, 1774–1783. https://doi.org/10.1002/jor.23445.

Baba, K., Mori, Y., Chiba, D., Kuwahara, Y., Kurishima, H., Tanaka, H., Kogure, A., Kamimura, M., Yamada, N., Ohtsu, S., Oyama, M., Masahashi, N., Hanada, S., Itoi, E., Aizawa, T., 2023. TiNbSn stems with gradient changes of Young's modulus and stiffness reduce stress shielding compared to the standard fit-and-fill stems. Eur. J. Med. Res. 28, 214. https://doi.org/10.1186/s40001-023-01199-z.

Beaupré, G.S., Orr, T.E., Carter, D.R., 1990. An approach for time-dependent bone modeling and remodeling-theoretical development: time-dependent modeling and remodeling. J. Orthop. Res. 8, 651–661. https://doi.org/10.1002/jor.1100080506.

Bennett, D., Goswami, T., 2008. Finite element analysis of hip stem designs. Mater. Des. 29, 45–60. https://doi.org/10.1016/j.matdes.2006.12.014.

Bugbee, W.D., Sychterz, C.J., Engh, C.A., 1996. Bone remodeling around cementless hip implants: South. Med. J. 89, 1036–1040. https://doi.org/10.1097/00007611-199611000-00002.

Chyr, A., Qiu, M., Speltz, J.W., Jacobsen, R.L., Sanders, A.P., Raeymaekers, B., 2014. A patterned microtexture to reduce friction and increase longevity of prosthetic hip joints. Wear 315, 51–57. https://doi.org/10.1016/j.wear.2014.04.001.

Cortis, G., Mileti, I., Nalli, F., Palermo, E., Cortese, L., 2022. Additive manufacturing structural redesign of hip prostheses for stress-shielding reduction and improved functionality and safety. Mech. Mater. 165, 104173. https://doi.org/10.1016/j.mechmat.2021.104173.

Cristofolini, L., Juszczyk, M., Taddei, F., Viceconti, M., 2009. Strain distribution in the proximal human femoral metaphysis. Proc. Inst. Mech. Eng. [H] 223, 273–288. https://doi.org/10.1243/09544119JEIM497.

Dammak, M., Shirazi-Adl, A., Zukor, D.J., 1997. Analysis of cementless implants using interface nonlinear friction - experimental and finite element studies. J. Biomech. 30, 121–129. https://doi.org/10.1016/S0021-9290(96)00110-8.

Engh, C., Bobyn, J., Glassman, A., 1987. Porous-coated hip replacement. The factors governing bone ingrowth, stress shielding, and clinical results. J. Bone Joint Surg. Br. 69–B, 45–55. https://doi.org/10.1302/0301-620X.69B1.3818732.

Fernandes, P.R., Folgado, J., Jacobs, C., Pellegrini, V., 2002. A contact model with ingrowth control for bone remodelling around cementless stems. J. Biomech. 35, 167–176. https://doi.org/10.1016/S0021-9290(01)00204-4.

Fraldi, M., Esposito, L., Perrella, G., Cutolo, A., Cowin, S.C., 2010. Topological optimization in hip prosthesis design. Biomech. Model. Mechanobiol. 9, 389–402. https://doi.org/10.1007/s10237-009-0183-0.

Gao, J.J., Thibon, I., Laillé, D., Castany, P., Gloriant, T., 2019. Influence of texture and transformation strain on the superelastic performance of a new Ti–20Zr–3Mo–3Sn alloy. Mater. Sci. Eng., A 762, 138075. https://doi.org/10.1016/j.msea.2019.138075.

Gillies, R.M., Kohan, L., Cordingley, R., 2007. Periprosthetic bone remodelling of a collum femoris preserving cementless titanium femoral hip replacement. Comput. Methods Biomech. Biomed. Eng. 10, 97–102. https://doi.org/10.1080/10255840601003577.

Grassi, L., Väänänen, S.P., Amin Yavari, S., Weinans, H., Jurvelin, J.S., Zadpoor, A.A., Isaksson, H., 2013. Experimental validation of finite element model for proximal composite femur using optical measurements. J. Mech. Behav. Biomed. Mater. 21, 86–94. https://doi.org/10.1016/j.jmbbm.2013.02.006.

Gruen, T.A., McNeice, G.M., Amstutz, H.C., 1979. "Modes of failure" of cemented stem-type femoral components: a radiographic analysis of loosening. Clin. Orthop. 17–27.

Hanada, S., Masahashi, N., Jung, T.-K., Yamada, N., Yamako, G., Itoi, E., 2014. Fabrication of a high-performance hip prosthetic stem using β Ti–33.6Nb–4Sn. J. Mech. Behav. Biomed. Mater. 30, 140–149. https://doi.org/10.1016/j.jmbbm.2013.11.002.

Harrison, N., McHugh, P.E., Curtin, W., Mc Donnell, P., 2013. Micromotion and friction evaluation of a novel surface architecture for improved primary fixation of cementless orthopaedic implants. J. Mech. Behav. Biomed. Mater. 21, 37–46. https://doi.org/10.1016/j.jmbbm.2013.01.017.

Head, W.C., Bauk, D.J., Emerson, R.H., 1995. Titanium as the material of choice for cementless femoral components in total hip arthroplasty. Clin. Orthop. 85–90.

Helgason, B., Perilli, E., Schileo, E., Taddei, F., Brynjólfsson, S., Viceconti, M., 2008. Mathematical relationships between bone density and mechanical properties: a literature review. Clin. Biomech. 23, 135–146. https://doi.org/10.1016/j.clinbiomech.2007.08.024.

Huiskes, R., Ruimerman, R., van Lenthe, G.H., Janssen, J.D., 2000. Effects of mechanical forces on maintenance and adaptation of form in trabecular bone. Nature 405, 704–706. https://doi.org/10.1038/35015116.

Huiskes, R., Weinans, H., Rietbergen, B.V., 1992. The relationship between stress shielding and bone resorption around total hip stems and the effects of flexible materials. Clin. Orthop. 274, 124–134. https://doi.org/10.1097/00003086-199201000-00014.

Jasty, M., Bragdon, C., Burke, D., O'connor, D., Lowenstein, J., Harris, W.H., 1997. In vivo skeletal responses to porous-surfaced implants subjected to small induced motions. J. Bone Jt. Surg. 79, 707.

Jetté, B., Brailovski, V., Simoneau, C., Dumas, M., Terriault, P., 2018. Development and in vitro validation of a simplified numerical model for the design of a biomimetic femoral stem. J. Mech. Behav. Biomed. Mater. 77, 539–550. https://doi.org/10.1016/j.jmbbm.2017.10.019.

Joshi, M.G., Advani, S.G., Miller, F., Santare, M.H., 2000. Analysis of a femoral hip prosthesis designed to reduce stress shielding. J. Biomech. 33, 1655–1662. https://doi.org/10.1016/S0021-9290(00)00110-X.

Kärrholm, J., Anderberg, C., Snorrason, F., Thanner, J., Langeland, N., Malchau, H., Herberts, P., 2002. Evaluation of a femoral stem with reduced stiffness. A randomized study with use of radiostereometry and bone densitometry. J. Bone Joint Surg. Am. 84, 1651–1658.

Kuiper, J.H., Huiskes, R., 1996. Friction and stem stiffness affect dynamic interface motion in total hip replacement. J. Orthop. Res. 14, 36–43. https://doi.org/10.1002/jor.1100140108.

Mjöberg, B., 1997. The theory of early loosening of hip prostheses. Orthopedics 20, 1169–1175. https://doi.org/10.3928/0147-7447-19971201-12.

Morgan, E.F., Unnikrisnan, G.U., Hussein, A.I., 2018. Bone mechanical properties in healthy and diseased states. Annu. Rev. Biomed. Eng. 20, 119–143. https://doi.org/10.1146/annurev-bioeng-062117-121139.

Moshfeghifar, F., Gholamalizadeh, T., Ferguson, Z., Schneider, T., Nielsen, M.B., Panozzo, D., Darkner, S., Erleben, K., 2022. LibHip: an open-access hip joint model repository suitable for finite element method simulation. Comput. Methods Progr. Biomed. 226, 107140. https://doi.org/10.1016/j.cmpb.2022.107140.

Naghavi, S.A., Tamaddon, M., Garcia-Souto, P., Moazen, M., Taylor, S., Hua, J., Liu, C., 2023. A novel hybrid design and modelling of a customised graded Ti-6Al-4V porous hip implant to reduce stress-shielding: an experimental and numerical analysis. Front. Bioeng. Biotechnol. 11.

Pilliar, R.M., Lee, J.M., Maniatopoulos, C., 1986. Observations on the effect of movement on bone ingrowth into porous-surfaced implants. Clin. Orthop. Relat. Res. 208, 108. 1976-2007.

Reimeringer, M., Nuño, N., 2016. The influence of contact ratio and its location on the primary stability of cementless total hip arthroplasty: a finite element analysis. J. Biomech. 49, 1064–1070. https://doi.org/10.1016/j.jbiomech.2016.02.031.

Rho, J.Y., Ashman, R.B., Turner, C.H., 1993. Young's modulus of trabecular and cortical bone material: ultrasonic and microtensile measurements. J. Biomech. 26, 111–119. https://doi.org/10.1016/0021-9290(93)90042-D.

Rivière, C., Grappiolo, G., Engh, C.A., Vidalain, J.-P., Chen, A.-F., Boehler, N., Matta, J., Vendittoli, P.-A., 2018. Long-term bone remodelling around 'legendary' cementless femoral stems. EFORT Open Rev. 3, 45–57. https://doi.org/10.1302/2058-5241.3.170024.

Shirazi-Adl, A., Dammak, M., Paiement, G., 1993. Experimental determination of friction characteristics at the trabecular bone/porous-coated metal interface in cementless implants. J. Biomed. Mater. Res. 27, 167–175. https://doi.org/10.1002/jbm.820270205.

Sun, C., Wang, L., Kang, J., Li, D., Jin, Z., 2018. Biomechanical optimization of elastic modulus distribution in porous femoral stem for artificial hip joints. J. Bionic Eng. 15, 693–702. https://doi.org/10.1007/s42235-018-0057-1.

Sychterz, C.J., Engh, C.A., 1996. The influence of clinical factors on periprosthetic bone remodeling. Clin. Orthop. Relat. Res. 322, 285.

Tanzer, M., Chan, S., Brooks, C.E., Bobyn, J.D., 2001. Primary cementless total hip arthroplasty using a modular femoral component: a minimum 6-year follow-up. J. Arthroplasty 16, 64–70. https://doi.org/10.1054/arth.2001.29140.

ten Broeke, R.H.M., Tarala, M., Arts, J.J., Janssen, D.W., Verdonschot, N., Geesink, R.G.T., 2014. Improving peri-prosthetic bone adaptation around cementless hip stems: a clinical and finite element study. Med. Eng. Phys. 36, 345–353. https://doi.org/10.1016/j.medengphy.2013.12.006.

Troelsen, A., Malchau, E., Sillesen, N., Malchau, H., 2013. A review of current fixation use and registry outcomes in total hip arthroplasty: the uncemented paradox. Clin. Orthop. Relat. Res. 471, 2052–2059. https://doi.org/10.1007/s11999-013-2941-7.

Van Rietbergen, B., Huiskes, R., Weinans, H., Sumner, D.R., Turner, T.M., Galante, J.O., 1993. The mechanism of bone remodeling and resorption around press-fitted THA stems. J. Biomech. 26, 369–382. https://doi.org/10.1016/0021-9290(93)90001-U.

Viceconti, M., Brusi, G., Pancanti, A., Cristofolini, L., 2006. Primary stability of an anatomical cementless hip stem: a statistical analysis. J. Biomech. 39, 1169–1179. https://doi.org/10.1016/j.jbiomech.2005.03.024.

Weinans, H., Huiskes, R., Grootenboer, H.J., 1992. Effects of material properties of femoral hip components on bone remodeling. J. Orthop. Res. 10, 845–853. https://doi.org/10.1002/jor.1100100614.

Weinans, H., R. Sumner, D., Igloria, R., Natarajan, R.N., 2000. Sensitivity of periprosthetic stress-shielding to load and the bone density–modulus relationship in subject-specific finite element models. J. Biomech. 33, 809–817. https://doi.org/10.1016/S0021-9290(00)00036-1.

Yamako, G., Chosa, E., Totoribe, K., Hanada, S., Masahashi, N., Yamada, N., Itoi, E., 2014. In-vitro biomechanical evaluation of stress shielding and initial stability of a low-modulus hip stem made of β type Ti-33.6Nb-4Sn alloy. Med. Eng. Phys. 36, 1665–1671. https://doi.org/10.1016/j.medengphy.2014.09.002.

Yamako, G., Janssen, D., Hanada, S., Anijs, T., Ochiai, K., Totoribe, K., Chosa, E., Verdonschot, N., 2017. Improving stress shielding following total hip arthroplasty by using a femoral stem made of β type Ti-33.6Nb-4Sn with a Young's modulus gradation. J. Biomech. 63, 135–143. https://doi.org/10.1016/j.jbiomech.2017.08.017.

Zhang, Y., Ahn, P.B., Fitzpatrick, D.C., Heiner, A.D., Poggie, R.A., Brown, T.D., 1999. Interfacial frictional behavior: cancellous bone, cortical bone, and a novel porous tantalum biomaterial. J. Musculoskelet. Res. 3, 245–251. https://doi.org/10.1142/S0218957799000269.